Acta Materialia 157 (2018) 288–297

Contents lists available at ScienceDirect

Acta Materialia

journal homepage: www.elsevier.com/locate/actamat

Controls on microstructural features during solidification of colloidal suspensions

Jiaxue You [a], Zhijun Wang [a], M. Grae Worster [b, *]

[a] State Key Laboratory of Solidification Processing, Northwestern Polytechnical University, Xi'an, 710072, China
[b] Department of Applied Mathematics and Theoretical Physics, University of Cambridge, Cambridge, CB3 0WA, United Kingdom

ARTICLE INFO

Article history:
Received 20 March 2018
Received in revised form
21 May 2018
Accepted 22 May 2018
Available online 17 July 2018

Keywords:
Solidification
Suspensions
Colloidal
Micro-structure

ABSTRACT

We present a mathematical model of the directional freezing of colloidal suspensions. Key ingredients of the model are the disjoining forces between the colloidal particles and the solidified suspending fluid, flow of the suspending fluid towards the solidification front through an accumulating layer of particles, and flow through microscopic films of unfrozen liquid separating particles from the freezing front. Our model predicts three different modes of solidification leading to different microstructures: dendritic formations; laddered structures of ice spears and lenses; a frozen fringe, from which transverse ice lenses can form. It explains why different researchers have reported the existence of ice lensing with and without the pre-existence of frozen fringes. Our quantitative predictions are encapsulated within a universal, dimensionless phase diagram showing which microstructure is to be expected under which operating conditions, and we show that these predictions are consistent with previous experimental studies as well as new experiments that we present here.

1. Introduction

Colloidal particles are forced into a variety of morphologies when a suspension is frozen [1,2]: soil is compacted between ice lenses during frost heave [3]; metal-matrix composites with tailored microstructure can be fabricated by freeze casting [4–7]; ice templating (freeze-casting using water as the suspending fluid) is a growing technology to produce bio-inspired, micro-porous materials [8–10]; cells and tissue can be damaged during cryo-surgery [11]; and the properties of phase change materials can be improved by nano-structures in thermal energy storage applications [12]. Commonly observed structures are ice lenses transverse to the direction of solidification (Fig. 1(a) and (b)) and dendrites aligned with the direction of solidification (Fig. 1 (c)). Whereas dendrites can be beneficial for cast materials, increasing compressive strength for example, lenses are generally deleterious to the mechanical properties of a casting. Our aim is to begin to develop a theoretical framework by which these different microstructures can be predicted.

Various studies have argued for and against the existence of *frozen fringes* (regions in which the suspending medium is frozen in the pores between particles) as necessary precursors of ice lenses [13,14]. Here, we provide a theoretical framework that identifies two different mechanisms for lens formation, with and without a frozen fringe, identifies the external parameters that differentiates between them and the possibility of dendritic formations, and unifies a range of apparently disparate conclusions drawn from previous experimental studies.

A colloidal suspension, in which the suspended particles are subject to Brownian diffusion, can be thought of as a type of binary alloy, the particles taking the role of the diffusing solute and the suspending fluid phase as the solvent [15,16]. In this article, we refer to the suspending fluid as water, since this is the most common in experiments, but the ideas extend to other fluids that premelt against the suspending solid. For example, lensing has been observed in soils saturated with benzene [17] and in silica saturated with argon [18]. Our theoretical understanding of the solidification of binary alloys is well-developed [19,20]. In particular, it is known under what conditions solid–liquid phase boundaries are morphologically unstable and give way to the formation of mushy regions of dendritic crystals of the primary solidifying phase [19,21]. By contrast, theories of solidification of colloidal suspensions are scarce [22]. Most fundamental studies have focused either on single particles being rejected or engulfed

* Corresponding author.
E-mail address: mgw1@cam.ac.uk (M. Grae Worster).

https://doi.org/10.1016/j.actamat.2018.05.049
1359-6454/

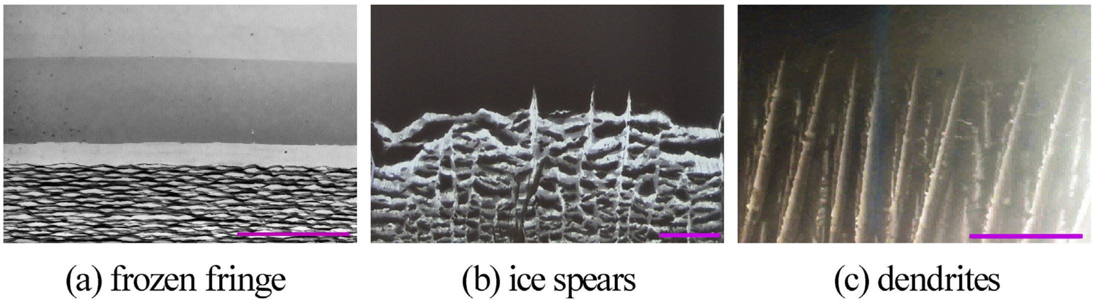

Fig. 1. Three typical patterns of solidification of colloidal suspensions: (a) frozen fringe; (b) ice spears; and (c) dendrites observed under different experimental conditions: (a) thermal gradient $G = 2.58$ K cm^{-1}, particle radius $a = 160$ nm, initial volume fraction of particles $\phi_0 = 27\%$, pulling speed $V = 1$ μm s^{-1}, scale bar 1 cm [27]; (b) $G = 2.25$ K cm^{-1}, $a = 160$ nm, $\phi_0 = 25\%$, $V = 7.33$ μm s^{-1}, scale bar 1 cm; (c) $G = 8.17$ K cm^{-1}, $a = 100$ nm, $\phi_0 = 27\%$, $V = 34.54$ μm s^{-1}, scale bar 0.5 mm. In (a), ice lenses are seen below a frozen fringe (white layer) that forms within a layer of consolidated particles (intermediate grey layer).

by an advancing solidification front [23,24] or on freezing the pore water within consolidated porous media [25–27]. The former is dominated by force balances and flow within a microscopically thin pre-melted liquid film separating the particle from the freezing solid (*film flow*), while the latter is dominated by fluid forces associated with flow through the porous medium (*Darcy flow*). The model we develop here incorporates both types of flow – Darcy flow through a consolidated layer of particles accumulating ahead of the freezing front and pre-melted film flow between the particles adjacent to the front and the front itself.

We describe our theoretical model in detail in Section 2. In Section 3, we describe our experiments of directionally freezing colloidal suspensions using polystyrene micro-spheres and alumina particles. In Section 4, we present a predicted phase diagram of different micro-structures and compare it with several experimental observations. Finally, two dimensionless parameters are identified that characterize the different micro-structural possibilities.

2. Theoretical model

The system we analyse is illustrated in Fig. 2. A layer of ice sits adjacent to a uniform suspension of colloidal particles, with volume fraction ϕ_0, within a linear temperature field $T(z) = T_m + Gz$, where T_m is the freezing temperature of the pure fluid phase

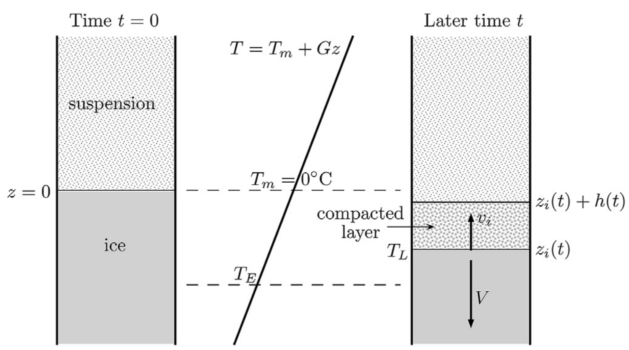

Fig. 2. Schematic diagram showing the system we analyse, which sits in a temperature gradient G established by fixed heat exchangers (not shown). At the initial time $t = 0$, a colloidal suspension of particle volume fraction ϕ_0 occupies the region $z > 0$ above a region of ice in $z < 0$. From $t = 0$ onwards, the system is pulled vertically downwards at speed V, towards lower temperatures, and ice grows upwards at speed $v_i \le V$. Therefore, in the frame of the heat exchangers, the ice front recedes to position $z_i(t) < 0$. Particles are initially rejected by the growing ice and compact to form a layer of thickness $h(t)$.

(0°C in the case of water) and G is the uniform temperature gradient. From an initial time $t = 0$, the system is pulled at speed V towards colder temperatures, which causes the water to freeze and rejected particles to accumulate ahead of the freezing front. The ice front $z = z_i(t)$ starts at the zero-degree isotherm $z = 0$ but recedes to negative values even as new ice is formed at rate $v_i < V$. The growing ice rejects the suspended particles, which forms a consolidated layer of thickness $h(t)$, the top of which is therefore at position $z_i(t) + h(t)$. Different modes of solidification, leading to different microstructures, occur depending on whether the top of the particle layer is above the zero-degree isotherm, $z_i(t) + h(t) > 0$, or below it, $z_i(t) + h(t) < 0$, and depending on when the ice front reaches the ice-entry isotherm $T = T_E$ at which the pore water between the consolidated particles begins to freeze. Note that the freezing temperature (liquidus) of a colloidal suspension is essentially the same as the freezing temperature of the suspending fluid for particles larger than about 10 nm unless the particles are compacted very close to each other.

There are two primary stresses involved in partially frozen suspensions of particles: one arising from thermo-molecular, disjoining forces between the ice and particles; the other arising from viscous flow. At a macroscopic level, the thermo-molecular pressure pushes the particles towards warmer temperatures, which drives the migration of liquid towards colder temperatures to sustain ice growth. At a microscopic level, this thermo-molecular pressure causes a thin pre-melted film to form between ice and particles at temperatures below the bulk freezing temperature. Liquid migrating from the far field to the freezing interface encounters a growing porous matrix and then the pre-melted film at the interface, which are called Darcy flow and film flow, respectively (see Fig. 3). By analyzing the disjoining forces and these two kinds of fluid flow, we build up a force-balance model of the growing concentrated particle layer.

2.1. Segregated ice versus pore ice

Two types of freezing ice must be distinguished: segregated ice and pore ice. A colloidal suspension is in equilibrium with bulk, segregated ice [22] when the osmotic pressure, defined by $\Pi(\phi) \equiv P - p$, is related to the temperature by

$$\Pi(\phi) \equiv P - p = \rho L \frac{T_m - T}{T_m}, \tag{1}$$

where ρ is the density of ice, L is the latent heat of fusion per unit mass, P is the total (bulk) pressure of the system, equal to any external loading, and p is the pore pressure of the suspending fluid

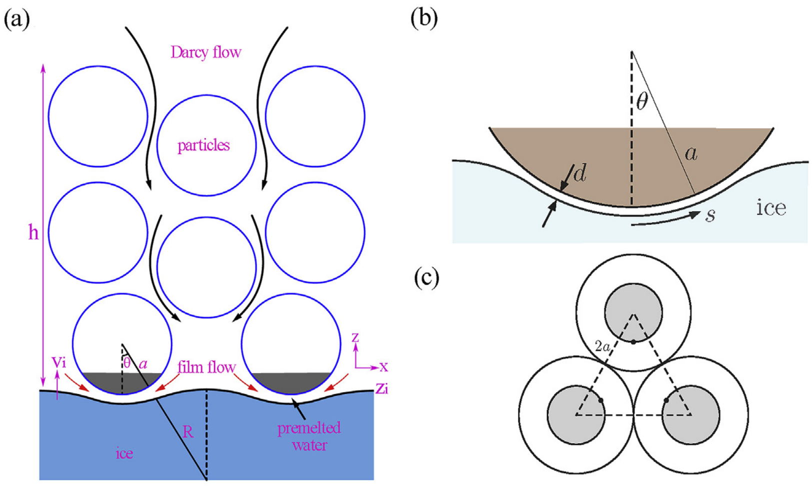

Fig. 3. (a) Schematic diagram of the fluid flow during solidification of colloidal suspensions, including Darcy flow and film flow. The diagram shows the thickness of the concentrated particle layer h, the speed of the ice interface v_i and its position z_i, a local angle θ measured from the centre of a particle and the radius of the particles a, and the radius of curvature of the free ice meniscus R. (b) Schematic diagram of the pre-melted film of thickness d between a spherical particle of radius a and ice. The arc length $s = a\theta$, where θ is the polar angle from the centre of the particle. (c) Plan view of three touching spherical particles of radius a and their associated pre-melted films (shaded grey) approximated as spherical caps extending to the points of tangency (dots) between the particles and a spherical ice cap of radius R.

measured relative to the (atmospheric) pressure p_0 at which the freezing temperature is T_m. In principle, external loading is provided by the weight of fluid and particles sitting above the ice, so the density of particles would have an influence on the quantitative results of our model if the system were vertical in a gravitational field. However, in laboratory settings, such hydrostatic pressures are typically small compared with the cryo-suction pressures governing these systems and any external loading (such as the weight of the consolidated particles) can be ignored. In natural settings, frost heave can be influenced by external loading ('overburden pressure') when the ice front sits beneath several metres of soil or beneath a building, for example. Here we consider the unloaded case $P = 0$, and equation (1) is equivalent to a liquidus relationship [28].

$$T = T_L \equiv T_m + \frac{T_m}{\rho L} p \tag{2}$$

between the freezing (liquidus) temperature T_L and the pore pressure. We refer to such regions of bulk ice as *segregated ice*.

On the other hand, ice can exist between particles if the temperature is below the ice-entry temperature [27].

$$T_E \equiv T_m - \frac{T_m}{\rho L}\frac{2\gamma}{R_f}, \tag{3}$$

where γ is the surface energy of an ice–water interface and $R_f = \lambda a$ is the radius of the largest sphere that can be inserted between particles. The constant λ can be determined analytically as $\lambda = \sqrt{3/2} - 1 \approx 0.225$ for hexagonally packed, precisely mono-disperse spheres of radius a but we use it here as an empirical constant, which has been found experimentally to lie in the range 0.2–0.6 [27] for almost mono-disperse particles of mean radius a. We refer to such ice as *pore ice* and to a region containing pore ice as a *frozen fringe*. Such a state is not in complete thermodynamic equilibrium but it can persist for very long times because the mobility of individual particles surrounded by pore ice is extremely small.

2.2. Disjoining forces

The dynamics and structure of the freezing system are determined by the interplay of forces and thermodynamics. While particles are completely rejected from an ice lens (Fig. 3(a)), the whole particle matrix is subject to the integrated disjoining force between the ice and its adjacent particles, which can be calculated most straightforwardly and accurately using ideas of thermodynamic buoyancy [25,29]. The principle of thermodynamic buoyancy, originally derived in Ref. [29] and analogous to Archimedes principle, says that the net thermomolecular force resulting from disjoining forces between ice and particles is proportional to the mass of 'displaced ice', being the density of ice times the volume of the system that is unfrozen while below 0 °C, independent of the particular intermolecular interactions that give rise to the disjoining forces. This principle gives the net thermomolecular force per unit area

$$p_T = \Delta\Theta \equiv \rho L \frac{T_m - T(z_i)}{T_m}, \tag{4}$$

where $\Delta\Theta$ is a scaled undercooling of the ice front at position z_i relative to the absolute bulk melting temperature of ice T_m, ρ is the density of ice and L is the latent heat of fusion. Note that this description is valid when considering scales much larger than the size of individual particles and that this net disjoining force does not depend on surface energy nor on the morphology of the freezing front.

2.3. Darcy flow

The disjoining force is resisted by viscous forces resulting from the flow of water through the porous layer of accumulated particles and through the premelted film beneath the particles adjacent to the ice front. The liquid pressure in the free pores of the particle layer adjacent to the ice front is the Darcy pore pressure p_D, which can be calculated from Darcy's equation [27].

$$\mu v_i = -k\frac{p_D - p_0}{h}, \tag{5}$$

where μ is the dynamic viscosity of water, v_i is the volume flux of water relative to the consolidated particles, which is equal to the freezing rate of the ice, p_0 is atmospheric pressure, which is equal to the pore pressure in the unconsolidated suspension, and h is the thickness of the layer of consolidated particles. The permeability k of the consolidated particle layer can be estimated using the Kozeny-Carmen equation

$$k = \frac{a^2 (1-\phi_p)^3}{45\phi_p^2}, \quad (6)$$

where ϕ_p is the volume fraction of particles, which are assumed to be random close-packed.

Equation (5) can be rearranged straightforwardly to give

$$p_D = p_0 - \frac{\mu h}{k} v_i. \quad (7)$$

2.4. Film flow

The flow in the pre-melted film can be approximated as parallel flow in a channel forming part of a spherical shell at the base of a particle, as shown in Fig. 3(b) [30]. Considering an axi-symmetric, three-dimensional situation, the volume flux q per unit arc length in the azimuthal direction is given by lubrication theory to be

$$q = \frac{-d^3}{12\mu} \frac{\partial p_l}{\partial s}, \quad (8)$$

where $p_l(s)$ is the liquid pressure in the pre-melted film, $s = a\theta$ is the arc length along a longitude of the spherical shell, a is the radius of the particles, θ is the polar angle measured from the downward vertical, μ is the dynamic viscosity of water and d is the thickness of the pre-melted film. This flux provides for the growth of ice at speed v_i according to

$$-2\pi a \sin\theta q = \pi a^2 \sin^2\theta \, v_i. \quad (9)$$

Combining equations (8) and (9), we obtain

$$\frac{\partial p_l}{\partial \theta} = \frac{6\mu a^2 v_i}{d^3} \sin\theta, \quad (10)$$

which can be integrated to give

$$p_l = p_D - \frac{6\mu a^2 v_i}{d^3} (\cos\theta - \cos\theta_c) \quad (11)$$

by applying the boundary condition that $p_l = p_D$ at the edge of the film, where $\theta = \theta_c$. The total upwards force under a single particle provided by the liquid pressure in the pre-melted film in excess of the Darcy pore pressure is therefore

$$F_f = \int_0^{\theta_c} 2\pi a \sin\theta \, (p_l - p_D) \cos\theta \, a d\theta = -\frac{2\pi\mu a^4 v_i}{d^3} \left(2 - 3\cos\theta_c + \cos^3\theta_c\right). \quad (12)$$

To determine the net additional contribution of the pre-melted films under many particles, consider the triangular unit cell shown in Fig. 3(b), of area $\sqrt{3}a^2$. This contains three sixths of the pre-melted films under adjacent particles, so the net force per unit area exerted by the liquid pressure within pre-melted films in excess of the Darcy pore pressure is

$$p_f = \frac{F_f/2}{\sqrt{3}a^2} = -\frac{\pi\mu a^2 v_i}{\sqrt{3}d^3} \left(2 - 3\cos\theta_c + \cos^3\theta_c\right). \quad (13)$$

For most of the transient evolution we consider, the freezing front is not significantly undercooled and a useful approximation can be made by considering the limit $R \gg a$, in which the radius of curvature of the free meniscus between particles is much larger than the radius of the particles. In this limit, we can approximate expression (13) by its Taylor expansion for small θ_c, noting that $2 - 3\cos\theta_c + \cos^3\theta_c \sim \frac{3}{4}\theta_c^4$.

Calculation of the film contribution p_f requires estimates for the film thickness d and extent θ_c. The thickness is determined from the generalised Clapeyron equation

$$\frac{A}{6\pi d^3} - \frac{2\gamma}{a} = \frac{\rho L}{T_m}(T_m - T_i) \equiv \Delta\Theta, \quad (14)$$

recognising that the pressure difference across the ice–water phase boundary is contributed to by the local disjoining force, with effective Hamaker constant A, and the surface energy (surface tension) γ.

The extent of the pre-melted film is determined by where the free meniscus is tangent to the spherical particles. The free meniscus has constant curvature $\kappa = 2/R$, where $R = 2/\kappa$ defines an equivalent radius of curvature equal to the radius of a sphere of curvature κ. The shape of the free meniscus is complicated in three dimensions and so we estimate the extent of the pre-melted film by considering the condition for tangency between a sphere of radius R and three neighbouring spherical particles of radius a, arranged as in Fig. 3(c). This approach gives the right parametric dependences for our overall formulae but will only approximate the associated geometrical coefficients. In this way, we estimate that

$$(R + a)\sin\theta_c = 2a/\sqrt{3}. \quad (15)$$

Note that $\theta_c \to \pi/2$ as $R/a \to 2/\sqrt{3} - 1$, which gives an extreme lower bound for $\lambda \approx 0.155$ above which the ice meniscus cannot be constrained even by a hexagonally-packed array of mono-dispersed particles. The radius R (really the curvature $2/R$) is determined from the generalised Clapeyron equation in the free region (the Gibbs-Thomson equation)

$$\frac{2\gamma}{R} = \Delta\Theta. \quad (16)$$

From equations (15) and (16) we see that when $R \gg a$

$$\theta_c \approx \frac{a}{\sqrt{3}\gamma} \Delta\Theta \quad (17)$$

and, from equation (14), that

$$\frac{A}{6\pi d^3} \approx \frac{2\gamma}{a}, \quad (18)$$

whence equation (13) can be estimated by

$$p_f \approx -\frac{\pi^2 \mu a^5 \Delta\Theta^4}{\sqrt{3} A \gamma^3} v_i. \quad (19)$$

2.5. Force balance and evolution equations

In the absence of any overburden pressure, the net force per unit area on the ice is atmospheric pressure, and the overall force balance can be expressed by

$$p_0 = p_T + p_D + p_f, \tag{20}$$

which can be written as

$$p_0 = \rho L \frac{T_m - T(z_i)}{T_m} + p_0 - \frac{\mu h}{k} v_i - \frac{\pi^2 \mu a^5 \Delta\Theta^4}{\sqrt{3} A \gamma^3} v_i \tag{21}$$

using equations (4), (7) and (19). This can be rearranged to give an equation for the freezing rate

$$\left[\frac{\mu h}{k} + \frac{\pi^2 \mu a^5 \Delta\Theta^4}{\sqrt{3} A \gamma^3}\right] v_i = \Delta\Theta, \tag{22}$$

recalling that

$$\Delta\Theta(z_i) = \rho L \frac{T_m - T(z_i)}{T_m}. \tag{23}$$

Once the freezing rate v_i is determined from (21), the position of the freezing front z_i and the thickness of the layer of consolidated particles h can be determined by integrating

$$\dot{z}_i = v_i - V, \qquad \dot{h} = \Phi v_i \tag{24}$$

starting at $z_i = h = 0$ at $t = 0$, where dots denote differentiation with respect to time, $\Phi = \phi_0/(\phi_p - \phi_0)$ and $\phi_p \approx 0.64$ is the volume fraction of close-packed particles.

2.6. Dimensionless equations and generic solutions

We scale lengths with respect to the distance $z_f = (T_m/\rho LG)(2\gamma/R_f)$ between the freezing isotherm $T = T_m$ and the isotherm corresponding to the ice-entry temperature $T = T_E$, and scale time with respect to z_f/V. With these scalings, equations (22) and (24) can be written in dimensionless form as

$$v_i = \frac{-z_i}{\mathscr{D} h + \mathscr{F} z_i^4}, \tag{25}$$

$$\dot{z}_i = v_i - 1, \qquad \dot{h} = \Phi v_i, \tag{26}$$

The Darcy coefficient $\mathscr{D} = \mu V T_m / k \rho L G$ is proportional to the ratio of the pressure drop across the porous medium $\Delta p_D = \mu V h/k$ to the cryosuction pressure drop $\rho L G h/T_m$, while the film coefficient $\mathscr{F} = (8\pi^2/\sqrt{3})\mu V a^2/A\lambda^3$ is proportional to the pressure drop in the pre-melted film beneath a particle $\Delta p_f = \mu a^2 V/d^3$ to the cryosuction pressure drop.

Equations (25) and (26) are singular at $t = 0$ but numerical integration can be initiated from the asymptotic solution $v_i \sim v_0 = (\sqrt{1 + 4\Phi\mathscr{D}} - 1)/2\Phi\mathscr{D}$ as $t \to 0$. An integration of these equations is shown in Fig. 4(b) and compared with measurements taken from a simple experiment in which all the particles were rejected at a planar ice front (Fig. 4(a)).

The more general behaviour of these equations is illustrated in Fig. 5. The thickness of the compacted particle layer and the position of the ice interface both evolve linearly at early times but the rate of thickening decreases to zero while the recession of the ice front increases to the pulling speed at large times once resistance in the premelted film dominates. Three different modes of behaviour can be identified.

If the ice front recedes below the ice-entry isotherm (z_i recedes below $z_i = -1$) while the top of the compacted layer is above the freezing isotherm ($z_i + h > 0$) then pore ice will form to create a frozen fringe, as seen in Ref. [27]. In this scenario, the decrease in pore-water pressure within the frozen fringe can cause the effective pressure between particles to decrease below zero and a new ice lens to form within the fringe [13,25,27] (Fig. 5(i)). The process begins again above the new ice front and repeats to form periodic ice lenses transverse to the temperature gradient. This is the case illustrated in Fig. 1(a).

If the top of the compacted layer recedes below the freezing isotherm, $z_i + h < 0$, the water both within and above the compacted layer becomes supercooled simultaneously. This is because the Darcy pressure field, which determines the liquidus temperature by equation (2), and the temperature field are both linear. We therefore predict that spears of ice will form from the ice lens,

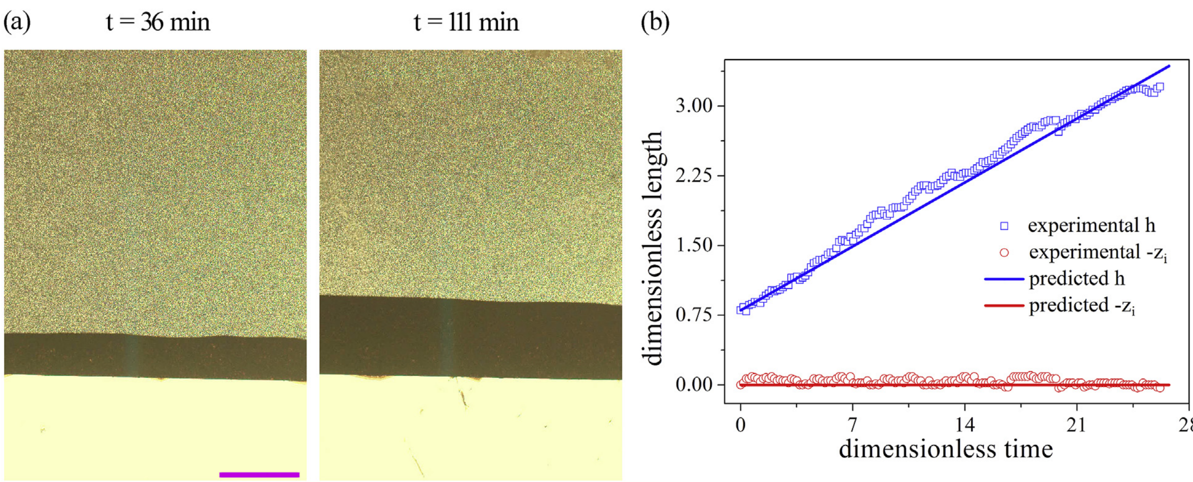

Fig. 4. (a) Experiments of directional freezing of suspensions of polystyrene beads of mean radius $a = 0.85\mu$m, showing complete particle rejection when the thermal gradient $G = 11.3$ K cm^{-1}, volume fraction of particles $\phi_0 = 0.057$ and pulling speed $V = 0.57\mu$m s^{-1}. The scale bar is 0.5 mm. (b) Experimental data and the predictions of our theory using $\lambda = 0.3$.

piercing the compacted layer to nucleate a new ice lens above it [28]. Equations (25) and (26) could then be re-initialised with respect to the new ice lens and thus a ladder-like structure is expected to develop with vertical ice spears forming the rails and horizontal ice lenses forming the rungs (see Fig. 1 (c) in Ref. [31]). If this happens while $z_i > -1$ then a laddered structure of ice lenses will develop without the formation of a frozen fringe (Fig. 5(ii) and 1(b)).

If $\mathscr{D} > 1 + \Phi$ then $-\dot{z}_i(0) > \dot{h}(0)$ and the system is immediately supercooled before any appreciable compacted layer forms. Supercooling of the liquid ahead of a solidification front in a binary alloy leads to morphological instability of the front, and we anticipate that the same will occur in these colloidal systems. Because the system is only supercooled locally to the front, we would additionally anticipate the development of cells leading to dendrites (Fig. 5(iii) and 1(c)), as also occurs in binary-alloy solutions. This contrasts with what we expect in the regime that leads to laddered structures, when the whole compacted layer and the region above it becomes supercooled simultaneously. No compaction of particles is expected above the mushy layer, and no ice lenses are expected to form.

From our theoretical model, the position of the ice front z_0 when the top of the compacted layer is at the zero-degree isotherm ($-z_0 = h$) determines the pattern of solidification: if $-z_0 > 1$ then a frozen fringe forms, out of which ice lenses may subsequently develop; if $0 < -z_0 < 1$ then a morphological instability is anticipated between the ice lens and the compacted layer that creates ice spears that penetrate the layer and nucleate a new ice lens above it; if $-z_0 = 0$ then a morphological instability is anticipated between the ice lens and the unconsolidated suspension to form a dendritic mushy layer. In Fig. 6, we show predictions of z_0 as functions of the pulling speed V, the thermal gradient G, the initial volume fraction of particles ϕ_0 and the radius of the particles a. We see that a sequence from frozen fringe to ice spears to dendritic mushy layer is predicted as the pulling speed increases, the gradient decreases, the volume fraction decreases or the particle radius decreases.

Our model deals with systems in which the thermodynamics of ice formation is dictated solely by the presence of particles and does not account for systems with significant dissolved solutes. In some studies (e.g. Refs. [16] [32]), ice lenses or ice bridges have been reported within dendritic mushy layers at high pulling speeds. The experiments reported in these studies included dissolved solutes and we speculate that dendritic mushy layers formed within them principally in consequence of the solutes, not the particles, and that thermal regelation of particle clusters within the mushy layer subsequently formed the ice bridges. If so then these observations are really distinct from the laddered structures that we have observed and model.

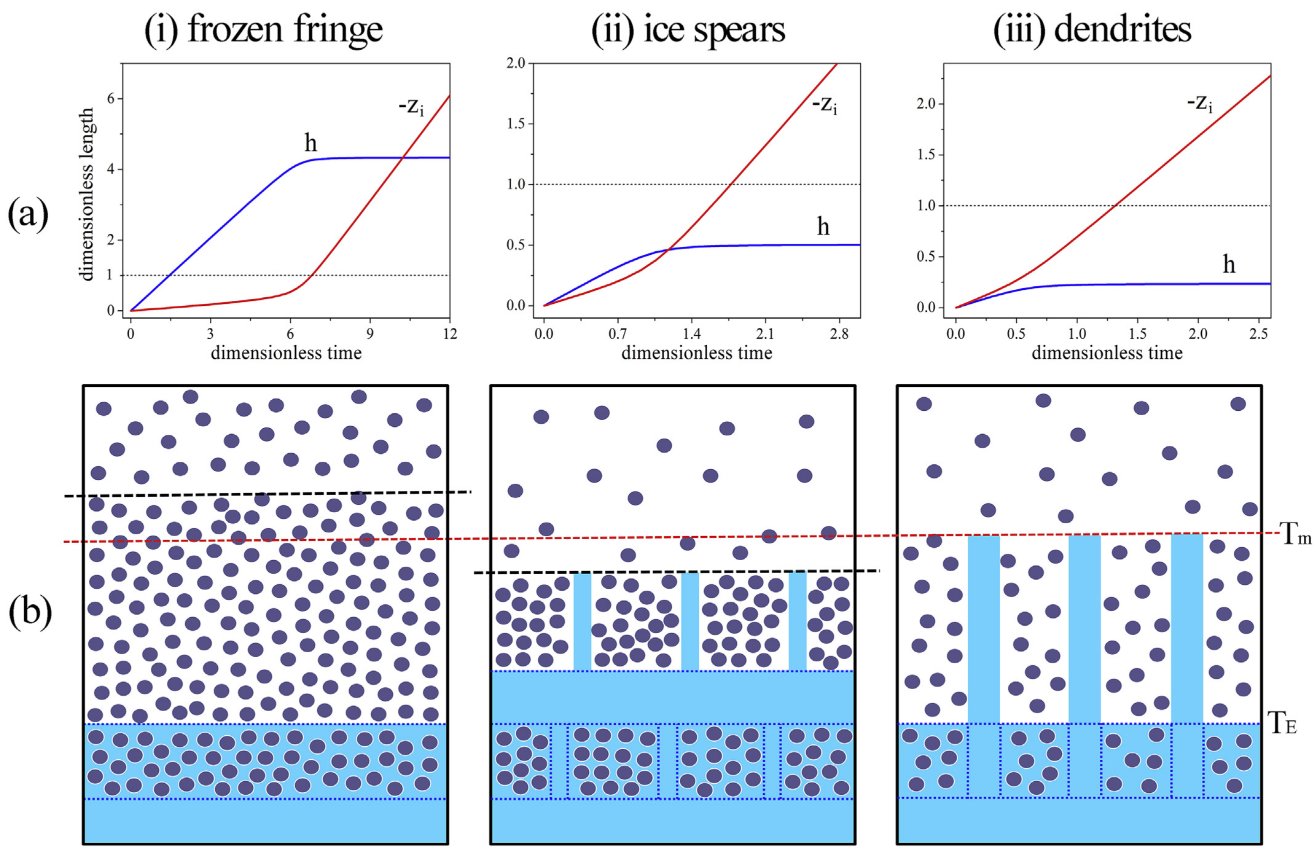

Fig. 5. Three typical patterns of solidification of colloidal suspensions: (i) frozen fringe; (ii) ice spears; and (iii) dendrites. (a) The dimensionless distance $-z_i$ (red curves) of the ice front below the zero-degree isotherm and the dimensionless thickness h of the consolidated layer of particles (blue curves) predicted by our theory. Position $-z_i = 1$ corresponds to where the temperature of the ice front is equal to the ice-entry temperature. (i) With $\mathscr{D} = 0.10$ and $\mathscr{T} = 5.14$, $-z_i$ reaches 1 while the layer of particles extends above the zero-degree isotherm, so a frozen fringe of pore ice forms within the consolidated layer. (ii) With $\mathscr{D} = 0.81$ and $\mathscr{T} = 37.71$, the top of the compacted layer of particles recedes below the zero-degree isotherm ($h < -z_i$) before $-z_i$ reaches 1, the interior of the layer and the suspension above the layer become supercooled, so ice spears and new ice lenses form a laddered structure. (iii) With $\mathscr{D} = 2.68$ and $\mathscr{T} = 69.40$, $-z_i > h$ immediately, so the suspension becomes supercooled and a dendritic mushy layer forms with no ice lenses. (b) Schematic illustrations of the evolutions described in (a). The position of the black dashed line is $z_i + h$. (For interpretation of the references to colour in this figure legend, the reader is referred to the Web version of this article.)

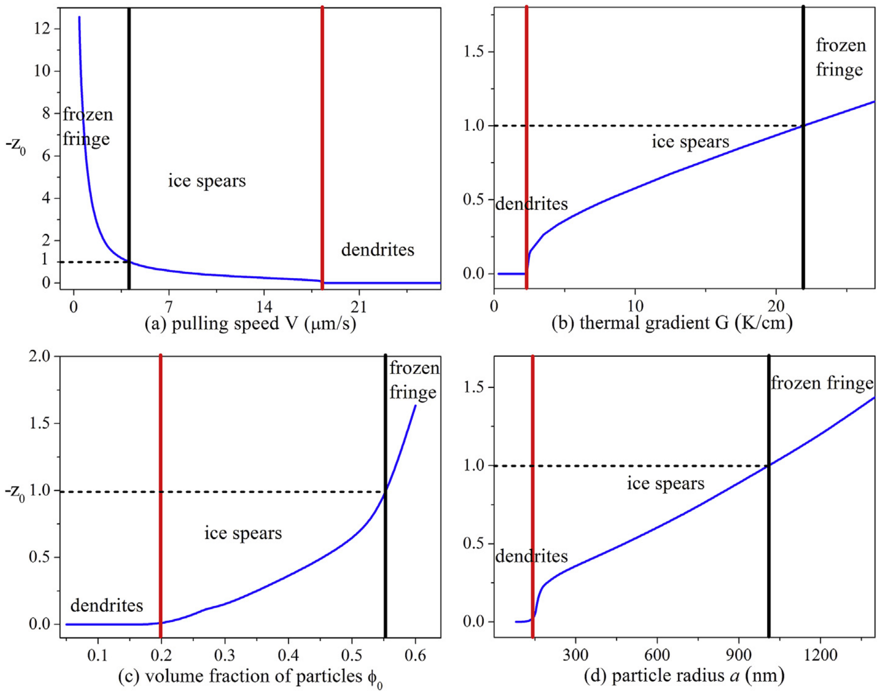

Fig. 6. Predictions of the position of the ice front when the top of the consolidated layer of particles recedes to the zero-degree isotherm, which determines whether a frozen fringe or ice spears or dendrites form. The values of parameters not being varied are the thermal gradient $G = 2.58$ K cm^{-1}, the volume fraction of particles $\phi_0 = 0.27$, the particle radius $a = 160$ nm and the pulling speed $V = 4$ μm s^{-1}, based on [27].

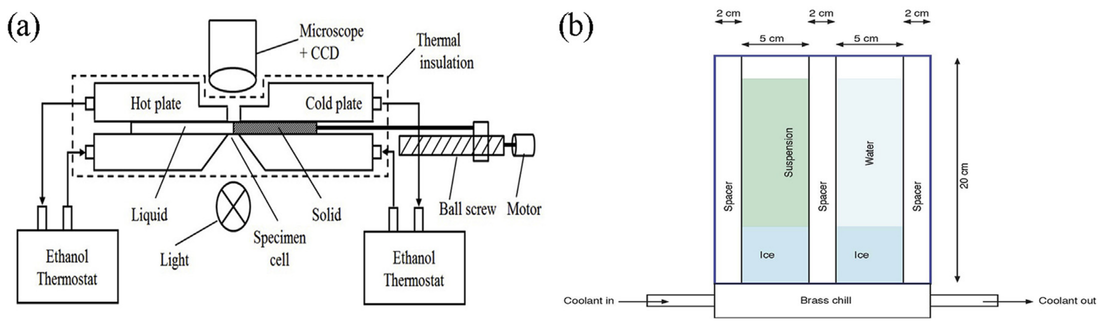

Fig. 7. (a) The Bridgman solidification apparatus used to produce the images in Fig. 1(c) and 4(a) and the data presented in Fig. 4(b) and 9 (labelled SM). (b) The one-sided cooling apparatus used to obtain the image in Fig. 1(b).

3. Experiments

Our model can also be used to make quantitative predictions of specific experiments. In the next section, we will show how our predictions are consistent with many previous experimental studies and also with some new experiments that we describe here. These experiments were conducted for different purposes but are collated here alongside other published experiments to provide additional tests of our model.

We used two different experimental facilities. The images in Figs. 1(c) and 4(a) and the data presented in Figs. 4(b) and 9 (labelled SM) come from an apparatus illustrated in Fig. 7(a). In this apparatus, a thermal gradient was produced by two heating and cooling zones separated by a gap of 5 mm. The temperatures of both heating and cooling zones were provided by ethanol thermostats whose temperatures could be maintained to an accuracy of $\pm 0.1\,^{\circ}$C at fixed values from $-20\,^{\circ}$C to $20\,^{\circ}$C by a temperature controller. The samples to be frozen were contained in rectangular glass cells (VitroCom) with dimensions $80 \times 2 \times 0.1$ mm^3 for the experiments shown in Fig. 1(c) and reported in Fig. 9[SM] and $80 \times 50 \times 0.3$ mm^3 for the experiments shown in Fig. 4. The cells were translated through the thermal gradient by a servo motor connected to a linear ball-screw drive. Observations of the growth front were made using an optical microscope stage with a charge-coupled device (CCD) camera. Further details of this apparatus are given in Ref. [33].

The image in Fig. 1(b) was taken in a simpler, larger apparatus, illustrated in Fig. 7(b). In this apparatus, two Hele-Shaw cells (internal dimensions $200 \times 50 \times 3$ mm^3) were arranged side by side above a fixed copper chill through which coolant (ethanol glycol) was circulated from a constant-temperature bath.

For the experiments shown in Figs. 1(b) and 8, we prepared alumina suspensions following [27]. Alumina powder (Alfa-Aesar, 99.95% purity) with mean particle diameter of either about 0.2 µm or about 0.32 µm was washed by deionized water and dispersed by adding a little HCl and applying ultrasonic pulsation (Branson Sonifier

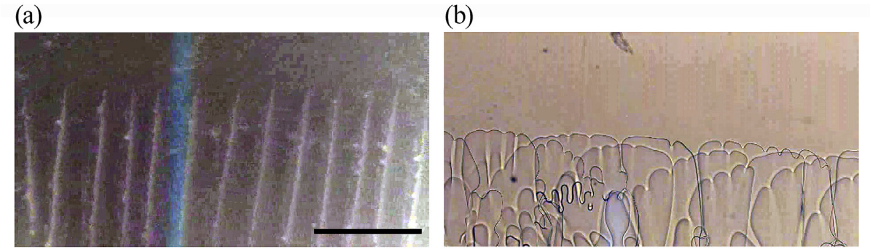

Fig. 8. (a) Directional solidification of an alumina suspension with $V = 27.9\ \mu m\ s^{-1}$, $G = 8.19\ K\ cm^{-1}$, $a = 100$ nm and $\phi_0 = 27\%$, showing the formation of dendrites. The scale bar is 0.5 mm. (b) Directional solidification of the supernatant alongside the experiment shown in (a), so under identical conditions but showing the formation of shallow cells.

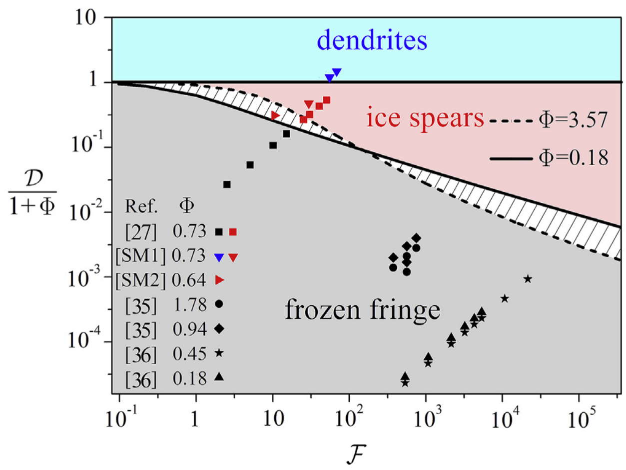

Fig. 9. A phase diagram showing the external dimensionless parameters $\mathscr{F}$, $\mathscr{D}/(1+\Phi)$ and Φ that determine the different styles of behaviour predicted by our theory. Superimposed on our theoretical phase diagram are the observations made by different experimentalists under different conditions. The colours indicate whether frozen fringes (black), ice spears (red) or dendrites (blue) were observed, while the shapes of the symbols indicate different experiments, as indicated in the key. Experiments SM1 and SM2 are our own experiments conducted using alumina particles. The physical parameters for all the experiments are tabulated in the Appendix. (For interpretation of the references to colour in this figure legend, the reader is referred to the Web version of this article.)

250) at 30 kHz for 10 min until the pH of the suspensions was 5. For the experiments shown in Fig. 4, we used polystyrene-microsphere (PS) suspensions, bought from the company Bangs Lab, USA. We diluted the original PS suspensions ($\phi_0 \sim 10.14\%$) to different initial volume fractions, as given in the relevant figure captions.

In this paper, we are highlighting the role of suspended particles in controlling the microscopic morphology of freezing suspensions but the morphology can, in principle, also be affected by solutes dissolved in the suspending fluid [33,34]. To ensure that we were observing the effects of particles, we ran our experiments in parallel with experiments in which the supernatant alone was frozen. The supernatant was obtained by centrifuging the particles out of the samples that were prepared for each experiment at 16,000 rpm for 20 min, after which there was essentially no particle debris. An illustration is given in Fig. 8, which contrasts the dendritic microstructure (strong morphological instability) formed in the particle-laden suspension with the shallow cells (weak morphological instability) formed in the supernatant. Our idealised theory accounts only for the effect of particles on the thermodynamics of the system and does not account for dissolved solutes. Had dissolved solutes been completely negligible in our experiments then the supernatant would have solidified with a stable, planar front.

4. Predicted microstructures

The findings illustrated in Fig. 6 are consolidated in Fig. 9, which shows which microstructure is expected depending on the external dimensionless parameters of the system $\mathscr{F}$, $\mathscr{D}$ and Φ. The cleanest delineation is achieved by plotting a phase diagram of $\mathscr{D}/(1+\Phi)$ versus $\mathscr{F}$, in which the division between dendrites and ice spears occurs precisely at $\mathscr{D}/(1+\Phi) = 1$ and the division between ice spears and frozen fringes depends only weakly on Φ. Overlain on this figure are indications of the observations made by several different experimental groups [27,35,36] and by ourselves (see previous section). The parameter values used to determine the data points in Fig. 9 are tabulated in the Appendix. We have chosen experiments that we assess to be dominated by particle interactions, not significantly influenced by dissolved solutes. The distinctions we have made between the different morphologies are qualitative or (in the case of existence of a frozen fringe or not) report what was identified in the associated literature. In some cases, such as those illustrated in Fig. 1, there is a clear distinction between (a) segregated ice forming structures (lenses) that are primarily perpendicular to the growth direction, (c) segregated ice forming structures (dendrites) that are parallel to the growth direction, and (b) segregated ice forming laddered or polygonal structures with significant features parallel and perpendicular to the growth direction. We see that all these observations are consistent with the predictions of our model.

It should be noted that there are other studies, not incorporated in Fig. 9, where the morphologies may not be so easily classified. For example [37], presents images of sintered samples that are lamellar in character but with occasional, fine bridges between lamellae. We would classify these images as ‘dendritic’, having a microstructure dominantly aligned with the growth direction. However, we have not included these results in Fig. 9 because the experiments contained significant additional solutes (dispersants and binders) that makes direct quantitative comparisons to our theory difficult.

5. Conclusions

The theoretical framework we have presented indicates how the micro-structural morphology of a frozen colloidal suspension can be tailored by varying the casting conditions. We have identified two significant, controlling dimensionless parameters: the Darcy Coefficient $\mathscr{D} = \mu V T_m / k\rho L G$; a Film Coefficient $\mathscr{F} = (8\pi^2/\sqrt{3})\mu V a^2 / A\lambda^3$, where μ, ρ and T_m are the viscosity, density and absolute freezing temperature of the suspending fluid, a is the radius of the suspended particles, L is the latent heat of fusion, G is the temperature gradient, V is the rate of solidification, A is an effective Hamaker constant between ice and particles, and λ is a geometrical coefficient that measures the degree of contact between ice and particles. There is a third dimensionless parameter $\Phi = \phi_0/(\phi_p - \phi_0)$, where ϕ_0 is the initial volume fraction of particles in the suspension and $\phi_p \approx 0.64$ is the volume fraction of close-packed particles, on which the systems depends only weakly. We note that the magnitude of the surface energy γ between ice and water determines the vertical length scale of macroscopic features but does not affect the type of microstructure observed.

Broadly speaking: dendrites parallel to the applied temperature gradient are expected when the Darcy Coefficient is large; frozen fringes leading to ice lenses transverse to the temperature gradient are expected when the Darcy Coefficient is much less than the Film Coefficient; and laddered structures comprising ice spears and connecting ice lenses are expected between these limits. A more precise division between these possibilities is given by the universal phase diagram (Fig. 9) that we have developed and quantified. The distinctions we have made between different morphologies observed in experiments are based on simple qualitative judgements and/or what was reported by the authors of the studies that we cite. One possibility for a more objective assessment, alongside more detailed future modelling, might be to take 2D Fourier Transforms of the images to determine the dominant directions of the microstructure.

Our model explains the observations made in laboratory experiments and paves the way to control pattern formations in complex solidification of colloidal suspensions and guide the development of new technologies and materials design [38].

Acknowledgements

This research was supported by Innovation Foundation for Doctor Dissertation in NWPU (CX201703) and National Natural Science Foundation of China (Grant No. 51701155). J.Y. thanks Xiaokang Ma for her dealing with all figures and Lilin Wang for discussion. It was conducted while J.Y. was a visiting scientist at DAMTP, University of Cambridge, funded by the British Council and China Scholarship Council.

Appendix

In Fig. 9, we have collated the data from several experimental studies, including our own, and compared them with our theoretical predictions. The physical parameters relevant to the data points in Fig. 9 are detailed below. The values we used for the Hamaker constants come from Ref. [39]. The value of λ we used (except in Table 4, which is from the published paper [35]) is from the geometrical prediction described in the main text.

Table 1
Data specific to experiments [27] using alumina

constant	value	units
ϕ_0	0.27	–
G	2.58	10^2 K m^{-1}
V	0.5, 1, 2, 3, 5, 6, 8, 10	10^{-6} m s^{-1}
a	160	10^{-9} m
A	3.67	10^{-20} J
λ	0.225	–

Table2
Data specific to experiments [SM1] using alumina

constant	value	units
ϕ_0	0.27	–
G	8.19	10^2 K m^{-1}
V	7.3, 27.9, 34.6	10^{-6} m s^{-1}
a	100	10^{-9} m
A	3.67	10^{-20} J
λ	0.225	–

Table 3
Data specific to experiments [SM2] using alumina

constant	value	units
ϕ_0	0.25	–
G	2.25	10^2 K m^{-1}
V	7.3	10^{-6} m s^{-1}
a	160	10^{-9} m
A	3.67	10^{-20} J
λ	0.225	–

Table 4
Data specific to experiments [35] using silica

constant	values	values	units
ϕ_0	0.31, 0.41	0.31, 0.41	–
G	2.8	4.8	10^2 K m^{-1}
V	1, 1.5, 2	1.5	10^{-6} m s^{-1}
a	0.75	0.75	10^{-6} m
A	0.46	0.46	10^{-20} J
λ	0.3	0.3	–

Table 5
Data specific to experiments [36] using polystyrene

constant	values	values	units
ϕ_0	0.2	0.1	–
G	4	4	10^3 K m^{-1}
V	0.5, 1, 2, 3, 4, 5, 10, 20	0.5, 1, 2, 3, 4, 5	10^{-6} m s^{-1}
a	1.5	1.5	10^{-6} m
A	1.55	1.55	10^{-20} J
λ	0.225	0.225	–

References

[1] S. Deville, E. Saiz, R.K. Nalla, A.P. Tomsia, Freezing as a path to build complex composites, Science 311 (2006) 515–518.
[2] J.G. Dash, A.W. Rempel, J.S. Wettlaufer, The physics of premelted ice and its geophysical consequences, Rev. Mod. Phys. 78 (2006) 695–741.
[3] J.S. Wettlaufer, M.G. Worster, Premelting dynamics, Annu. Rev. Fluid Mech. 38 (2006) 427–452.
[4] C. Ferraro, S. Meille, J. RÃ©thorÃ©, N. Ni, J. Chevalier, E. Saiz, Strong and tough metal/ceramic micro-laminates, Acta Mater. 144 (2018) 202–215.
[5] F. Bouville, E. Maire, S. Meille, B. Van de MoortÃle, A.J. Stevenson, S. Deville, Strong, tough and stiff bioinspired ceramics from brittle constituents, Nat. Mater. 13 (2014) 508–514.
[6] M. Naviroj, P.W. Voorhees, K.T. Faber, Suspension- and solution-based freeze casting for porous ceramics, J. Mater. Res. 32 (2017) 3372–3382.
[7] S.A. Barr, E. Luijten, Structural properties of materials created through freeze casting, Acta Mater. 58 (2010) 709–715.
[8] T. Waschkies, R. Oberacker, M.J. Hoffmann, Investigation of structure formation during freeze-casting from very slow to very fast solidification velocities, Acta Mater. 59 (2011) 5135–5145.
[9] U.G.K. Wegst, H. Bai, E. Saiz, A.P. Tomsia, R.O. Ritchie, Bioinspired structural materials, Nat. Mater. 14 (2015) 23–26.
[10] K.L. Scotti, E.E. Northard, A. Plunk, B.C. Tappan, D.C. Dunand, Directional solidification of aqueous *Tio*$_2$ suspensions under reduced gravity, Acta Mater. 124 (2017) 608–619.
[11] Z. Xia, X. Yu, X. Jiang, H.D. Brody, D.W. Rowe, M. Wei, Fabrication and characterization of biomimetic collagen–apatite scaffolds with tunable structures for bone tissue engineering, Acta Biomater. 9 (2013) 7308–7319.
[12] Y.M.F. El Hasadi, J.M. Khodadadi, One-dimensional Stefan problem formulation for solidification of nanostructure-enhanced phase change materials (NePCM), Int. J. Heat Mass Tran. 67 (2013) 202–213.
[13] K. O'Neill, R.D. Miller, Exploration of a rigid ice model of frost heave, Water Resour. Res. 21 (1985) 281–296.
[14] K. Watanabe, M. Mizoguchi, Ice configuration near a growing ice lens in a freezing porous medium consisting of micro glass particles, J. Cryst. Growth 213 (2000) 135–140.
[15] S.S.L. Peppin, J.S. Wettlaufer, M.G. Worster, Experimental verification of morphological instability in freezing aqueous colloidal suspensions, Phys. Rev. Lett. 100 (2008) 238301.

[16] S. Deville, E. Maire, G. Bernard-Granger, A. Lasalle, A. Bogner, C. Gauthier, J. Leloup, C. Guizard, Metastable and unstable cellular solidification of colloidal suspensions, Nat. Mater. 8 (2009) 966–972.
[17] S. Taber, The mechanics of frost heaving, J. Geol. 38 (4) (1930) 303–317.
[18] D-M. Zhu, J.G. Dash, B. Sing, O.E. Vilches, J.S. Wettlaufer, Frost heave in argon, Phys. Rev. Lett. 85 (2000) 4908.
[19] M.G. Worster, Solidification of fluids, in: G.K. Batchelor, H.K. Moffatt, M.G. Worster (Eds.), Perspectives in Fluid Dynamics – a Collective Introduction to Current Research, Cambridge University Press, 2000, pp. 393–446.
[20] S.H. Davis, Theory of Solidification, Cambridge University Press, 2001.
[21] W.W. Mullins, R.F. Sekerka, Stability of a planar interface during solidification of a dilute binary alloy, J. Appl. Phys. 35 (1964) 444–451.
[22] S.S.L. Peppin, J.A.W. Elliott, M.G. Worster, Solidification of colloidal suspensions, J. Fluid Mech. 554 (2006) 147–166.
[23] R.R. Gilpin, A model of the "liquid-like" layer between ice and a substrate with applications to wire regelation and particle migration, J. Colloid Interface Sci. 68 (1979) 235–251.
[24] A.W. Rempel, M.G. Worster, The interaction between a particle and an advancing solidification front, J. Cryst. Growth 205 (3) (1999) 427–440.
[25] A.W. Rempel, J.S. Wettlaufer, M.G. Worster, Premelting dynamics in a continuum model of frost heave, J. Fluid Mech. 498 (2004) 227–244.
[26] R.W. Style, S.S.L. Peppin, The kinetics of ice-lens growth in porous media, J. Fluid Mech. 692 (2012) 482–498.
[27] A.M. Anderson, M.G. Worster, Periodic ice banding in freezing colloidal dispersions, Langmuir 28 (48) (2012) 16512–16523.
[28] R.W. Style, S.S.L. Peppin, A.C.F. Cocks, J.S. Wettlaufer, Ice-lens formation and geometrical supercooling in soils and other colloidal materials, Phys. Rev. E 84 (2011) 1–12.
[29] A.W. Rempel, J.S. Wettlaufer, M.G. Worster, Interfacial premelting and the thermomolecular force: thermodynamic buoyancy, Phys. Rev. Lett. 8708 (8) (2001) 8501.
[30] M.G. Worster, J.S. Wettlaufer, The fluid mechanics of premelted liquid films, in: W. Shyy (Ed.), Fluid Dynamics at Interfaces, Cambridge University Press, 1999, pp. 339–351.
[31] S.S.L. Peppin, M.G. Worster, J.S. Wettlaufer, Morphological instability in freezing colloidal suspensions, Proc. R. Soc. A 463 (2007) 723–733.
[32] A. Lasalle, C. Guizard, E. Maire, J. Adrien, S. Deville, Particle redistribution and structural defect development during ice templating, Acta Mater. 60 (11) (2012).
[33] J. You, L. Wang, Z. Wang, J. Li, J. Wang, X. Lin, W. Huang, In situ observation the interface undercooling of freezing colloidal suspensions with differential visualization method, Rev. Sci. Instrum. 86 (2015) 084901.
[34] J. You, L. Wang, Z. Wang, J. Li, J. Wang, X. Lin, W. Huang, Interfacial undercooling in solidification of colloidal suspensions: analyses with quantitative measurements, Sci. Rep. 6 (2016) 28434.
[35] J.M.H. Schollick, R. Style, A. Curran, J.S. Wettlaufer, E.R. Dufresne, P.B. Warren, K.P. Velikov, R.P.A. Dullens, D.G.A.L. Aarts, Segregated ice growth in a suspension of colloidal particles, J. Phys. Chem. B 120 (16) (2016) 3941–3949.
[36] B. Saint-Michel, M. Georgelin, S. Deville, A. Pocheau, Interaction of multiple particles with a solidification front: from compacted particle layer to particle trapping, Langmuir 33 (23) (2017) 5617–5627.
[37] S. Deville, E. Saiz, A.P. Tomsia, A. P, Ice-templated porous alumina structures, Acta Mater. 55 (6) (2007) 1965–1974.
[38] Q. Cheng, C. Huang, A.P. Tomsia, Freeze casting for assembling bioinspired structural materials, Adv. Mater. 1703155 (2017) 1–11.
[39] L. Bergström, Hamaker constants of inorganic materials, Adv. Colloid Interfac. 70 (1997) 125–169.